applied sciences

MDPI

Article

Capacity-Operation Collaborative Optimization for Wind-Solar-Hydrogen Multi-Energy Supply System

Lintong Liu [1], Rongrong Zhai [1,*], Yangdi Hu [1], Hang Yin [2], Qiang Wang [2], Yu Xu [1] and Chongbao Sun [1]

[1] School of Energy Power and Mechanical Engineering, North China Electric Power University, Beijing 100096, China; liulintong1994@163.com (L.L.); huyangdi0309@163.com (Y.H.); xy15703421187@163.com (Y.X.); cb17863908520@163.com (C.S.)

[2] China General Nuclear Power New Energy Holding Co., Ltd., Beijing 100071, China; yinhang36@163.com (H.Y.); 15911108785@163.com (Q.W.)

* Correspondence: zhairongrong01@163.com

Abstract: In pursuit of widespread adoption of renewable energy and the realization of decarbonization objectives, this study investigates an innovative system known as a wind-solar-hydrogen multi-energy supply (WSH-MES) system. This system seamlessly integrates a wind farm, photovoltaic power station, solar thermal power station, and hydrogen energy network at the power grid level. Central to the study is the introduction of a bi-level collaborative optimization model—an innovative algorithmic framework specifically tailored for complex multi-energy systems. This model co-optimizes both the capacity planning of essential system components and their annual load distribution, adeptly navigating the complexities of optimizing capacity and annual load distribution under uncertain energy sources and load conditions. A layered methodology synergistically combines linear programming with an advanced version of non-dominated sorting genetic algorithm-II. When applied to a real-world case study in Zhangbei, China, this approach identifies an optimal system capacity, leading to annual green power generation of 201.56 GW and a substantial reduction of over 173,703 tons of CO_2 emissions. An economic analysis further reveals that each 1% reduction in CO_2 emissions corresponds to a modest 1.7% increase in the system's levelized cost of energy. Moreover, a comprehensive exploration of the impacts of various capacity parameters on the WSH-MES system's performance is conducted. These insights offer invaluable guidance for the large-scale advancement of efficient renewable energy utilization and the attainment of decarbonization targets.

Keywords: wind/photovoltaic/concentrating solar power/proton exchange membrane electrolysis/proton exchange membrane fuel cell; multi-energy supply system; capacity-operation collaborative optimization; multi-objective optimization; sensitivity analysis

check for updates

Citation: Liu, L.; Zhai, R.; Hu, Y.; Yin, H.; Wang, Q.; Xu, Y.; Sun, C. Capacity-Operation Collaborative Optimization for Wind-Solar-Hydrogen Multi-Energy Supply System. *Appl. Sci.* **2023**, *13*, 11011. https://doi.org/10.3390/app131911011

Academic Editor: Alejandro Pérez-Rodríguez

Received: 9 August 2023
Revised: 10 September 2023
Accepted: 24 September 2023
Published: 6 October 2023

1. Introduction

The widespread deployment and harnessing of renewable energy sources hold the potential to diversify energy markets, secure long-term energy sustainability, and significantly mitigate both local and global carbon dioxide emissions [1]. Yet, these renewable sources are not without their challenges, including pronounced seasonal fluctuations in wind and hydropower availability [2], as well as the lack of electricity generation during night-time hours for photovoltaic (PV) and concentrated solar power (CSP) installations [3]. To surmount these limitations, the advancement of integrated multi-energy supply systems and their orchestrated operation emerges as a compelling strategy to enhance energy efficiency, alleviate looming energy crises, and mitigate environmental degradation.

Currently, there is extensive research into distributed energy systems that rely on complementary energy time scales of various energy sources. These systems have reached the level of scaled-up applications to some extent [4,5]. New varieties of CSP-based hybrid renewable energy systems, such as CSP-wind [6] and CSP-PV-wind [7] systems, have been investigated. As wind and solar energy are renewable energy sources with significant volatility [8], coupling CSP power generation with wind power (WP) and PV power generation can achieve high-quality power output. This approach leverages the inherent stability, continuity, and dispatchability of CSP to temper the fluctuations of WP and PV [9], while also channeling excess wind and solar energy into thermal storage, thereby minimizing waste [10]. Nevertheless, the finite capacity of thermal energy storage (TES) systems still leaves a considerable amount of unutilized power. Therefore, when excess energy is generated, the parallel production of clean fuels like hydrogen presents an advantageous route. Utilizing renewable energy sources for hydrogen production not only mitigates pollution by reducing dependence on fossil fuel combustion [11] but also enhances system energy efficiency by providing an alternative use for excess wind and solar energy [12]. Therefore, the integration of various subsystems into the hybrid renewable energy configuration can significantly boost overall efficiency. For instance, hydrogen production through proton exchange membrane electrolysis (PEME) [13,14] and power generation using integrated proton exchange membrane fuel cells (PEMFC) [15,16] have shown notable results. Specifically, Xu et al. [14] optimized a wind/PV/hydrogen system, achieving a levelized cost of energy (LCOE) as low as 0.226 USD/kWh. Similarly, Tao et al. [16] introduced an innovative combination of an organic flash cycle and PEMFC for poly-generation purposes, attaining an energy efficiency of 25.47% after multi-objective optimization.

Based on the new developed system, researchers have made significant progress in analyzing the system from various perspectives such as energy, exergy, economy, and environmental (4E) aspects. The 4E analysis has gained substantial attention from academics as a promising analytical method for evaluating the performance of various energy systems [17–19]. For instance, Mohamed et al. [20] undertook a comprehensive 4E assessment of a hybrid hydrogen system, revealing energy and exergy efficiencies of 16.42% and 12.76%, respectively. Similarly, Kalinci et al. [21] probed into the feasibility of hydrogen generation from electrolytic water within a hybrid energy system, reporting an average daily hydrogen yield of 1.49 kg/h in the Turkey region. Further enriching the literature, Abbas Alpaslan Kocer [22] executed rigorous thermodynamic scrutiny, environmental impact assessment, and parametric studies on a solar- and wind-energy-integrated power and hydrogen production system. Complementing these theoretical endeavors, field studies focusing on renewable energy and hydrogen production have also been conducted, offering invaluable insights for policy makers and investors to judiciously evaluate renewable energy adoption and site selection strategies [23].

Optimizing and efficiently operating systems can significantly enhance their performance [24–26]. Extensive research has been conducted on the optimization of multi-energy systems (MES), focusing on objectives like energy, economy, and the environment. The primary decision variable is often the equipment capacity. While the majority of studies prioritize single-objective optimization centering on economic feasibility, other factors such as efficiency, reliability, and environmental protection are equally vital in determining system operability [27]. Multi-objective programming addresses these considerations, especially in MES, where reducing pollution and improving reliability might mean compromising on economic feasibility to some extent [28]. Liu et al. [29] used the genetic-algorithm–particle-swarm optimization to optimize the nominal PV, system power output point, and thermal energy storage capacity of a thermal-storage PV-CSP system for various scheduling strategies, aiming to achieve the most cost-effective electricity level. Fang [30] developed an integrated energy system incorporating hydrogen storage and performed a multi-objective optimization focusing on carbon emissions and operational costs. This study revealed that multi-objective optimization outperformed its single-objective counterpart. The system's operating strategy also plays a pivotal role in the performance of MES [31]. Zhang et al. [32] introduced an enhanced operating strategy rooted in an electric heating load following and optimized the system using the Artificial Bee Colony Algorithm. They then compared optimization results across four variable operating strategies to identify the most effective one. Meanwhile, Ding et al. [33] incorporated load scheduling into the multi-objective capacity optimization process, executing a capacity operation collaborative optimization for a solar-assisted coal-fired cogeneration system. Their aim was to strike the right balance between economic considerations and carbon emissions. Their method provided insights into the primary capacity and the system's annual load scheduling. A comparative analysis between this study and the referenced research can be found in Table 1.

Table 1. The method proposed in this paper is compared with other literature.

Reference	System Composition		Optimization						
	Renewable Energy	Storage Units	Economy	Carbon Emissions	Source and Load Uncertainty	Operation Strategy	Collaborative Optimization	Multi-Objective	Multiple Solving Algorithms
[24]	×	√	√	√	×	×	×	√	×
[25]	×	√	√	√	√	×	×	√	√
[26]	×	√	√	×	×	√	×	√	×
[28]	×	√	√	√	×	×	×	√	×
[29]	√	√	√	×	×	√	×	×	×
[30]	√	×	√	√	×	√	×	√	×
[31]	√	×	×	×	×	×	×	√	√
[32]	×	×	×	√	√	√	×	√	×
[33]	×	√	√	√	×	√	√	√	×
Proposed	√	√	√	√	√	√	√	√	√

In the table, "√" represents what has been studied in the relevant literature, "×" represents research gaps in the literature.

From a literature review perspective, a limited number of researchers have delved into the energy supply constraints of multi-source energy systems powered exclusively with renewable energy. Notably, few proposed systems have been designed to use CSP-wind-PV-PEMFC collectively for energy supply, while concurrently harnessing surplus energy for green hydrogen production, ensuring a consistent electrical output. Existing research primarily emphasizes integration methods and performance evaluations, often sidelining capacity and operational optimization. Furthermore, previous endeavors typically focused on the individual optimization of capacity and load scheduling for major components in systems connected to renewable energy sources. However, for determining the optimal capacity configuration, a combined approach to capacity operation is imperative. This is because load scheduling and capacity configuration are closely inter-related, influencing one another.

Additionally, the wind-solar-hydrogen multi-energy supply (WSH-MES) system exhibits a sophisticated architecture. It encompasses diverse energy conversion pathways and mechanisms within its core processes, encompassing both photovoltaic–thermal and established thermal cycle energy conversion methods. Notably, the system is subject to the influence of meteorological conditions and user load requirements [24,33,34]. Remarkably, the factor of uncertainty stemming from this intricate interplay between energy source and load demand has been notably absent in prior system optimization investigations. This is particularly relevant for systems that are exclusively reliant on renewable energy sources.

To fill the gaps in the previous studies, a capacity-operating co-optimization model that considers source-load uncertainty in the optimization process is proposed. The model utilizes multi-objective optimization with carbon emissions and economic objectives and optimizes the annual load plan and system's main component capacity. This is mentioned in the outlook of many studies [24,33], but it has not been resolved. The present study is a further extension of previous studies [35–37] and the new contributions are as follows:

(1) A novel WSH-MES system combining electricity, hydrogen, heating, and storage is constructed, which is fully driven with renewable energy and optimizes its capacity in the face of source load uncertainty.

(2) A bi-level capacity-operation collaborative optimization model considering the uncertainty of source and load that integrates reliability, environmental protection, and

economy is established. The model is solved using non-dominated sorting genetic algorithm-II (NSGA-II) and linear programming (LP).

(3) A comprehensive analysis is conducted to reveal the effects of capacity parameters on the performance of the WSH-MES system.

2. System Description

2.1. WSH-MES System

Figure 1 illustrates the sophisticated WSH-MES system, a composite of five unique subsystems: PV, WP, CSP, PEME, and PEMFC.

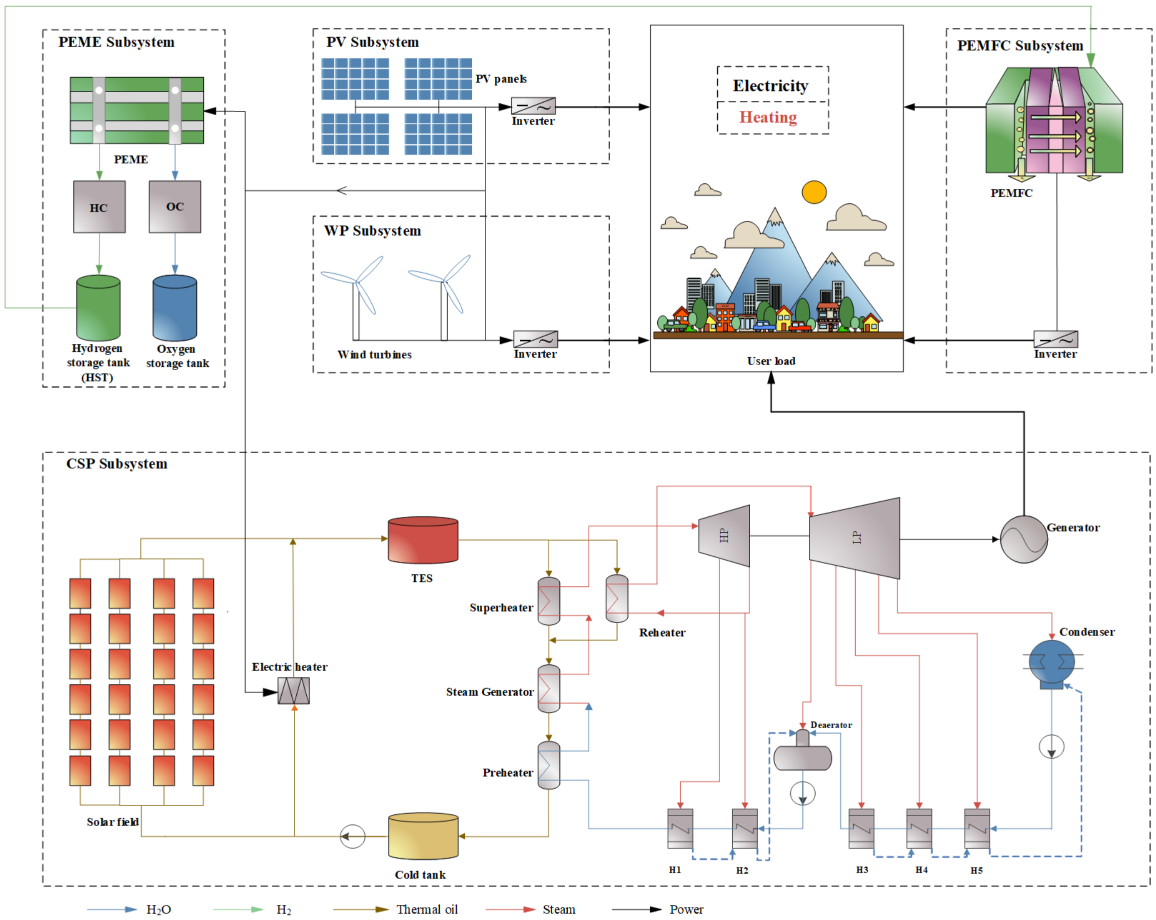

Figure 1. Diagram of WSH-MES system.

PV and WP Subsystems: These subsystems primarily supply electricity to consumers. Surplus power is directed to the PEME subsystem for the conversion into hydrogen. Both subsystems include inverters, with the PV subsystem consisting of solar panels and the WP subsystem containing a wind turbine. The electrical outputs from the solar panels and wind turbine are connected to the PEME subsystem and the users through their respective inverters.

CSP and PEMFC Subsystems: Serving as peak power sources, they share the electrical load with the PV and WP subsystems, ensuring a balanced energy distribution.

PEME Subsystem: Specialized in hydrogen production, the hydrogen generated here is used in the PEMFC subsystem to create electricity.

CSP Subsystem Components: This subsystem encompasses a solar field (SF), electric heater (EH), hot salt tank, superheater, steam generator, preheater, cold salt tank, high-pressure cylinder, low-pressure cylinder, and steam turbine. The SF's heat transfer end connects to the hot salt tank, and the latter's high-temperature molten salt output links to the superheater, steam generator, preheater, and cold salt tank. Together, these elements heat the feed water, producing superheated steam for the high-pressure cylinder. The cold salt tank's chilled molten salt output feeds into the SF, and the steam from the high-pressure cylinder flows to the low-pressure cylinder, driving the steam turbine and generator to deliver electricity to the user.

2.2. Operation Strategy

A carefully orchestrated energy management strategy is vital for handling the inherent fluctuations of renewable energy sources such as wind and solar and to adapt to changes in user load demands effectively. The WSH-MES system is engineered to offer an encompassing solution to these complexities. In this framework, power generated with PV panels and WP systems serves as the primary electricity source. Their output is directed to meet immediate user demands, thus minimizing any need to rely on non-renewable sources, as indicated in Figure 1.

When an excess of power is generated with these renewable sources, it triggers a set of energy storage solutions. Initially, the surplus electricity is used for electrolysis to produce hydrogen, which is then stored in the HST system. The HST serves as a robust chemical energy storage solution, also highlighted in Figure 2. Should there still be excess power after the HST system is at full capacity, this additional power is converted into thermal energy for subsequent storage in the TES system. The TES system is designed to store energy that can later be used for heating applications.

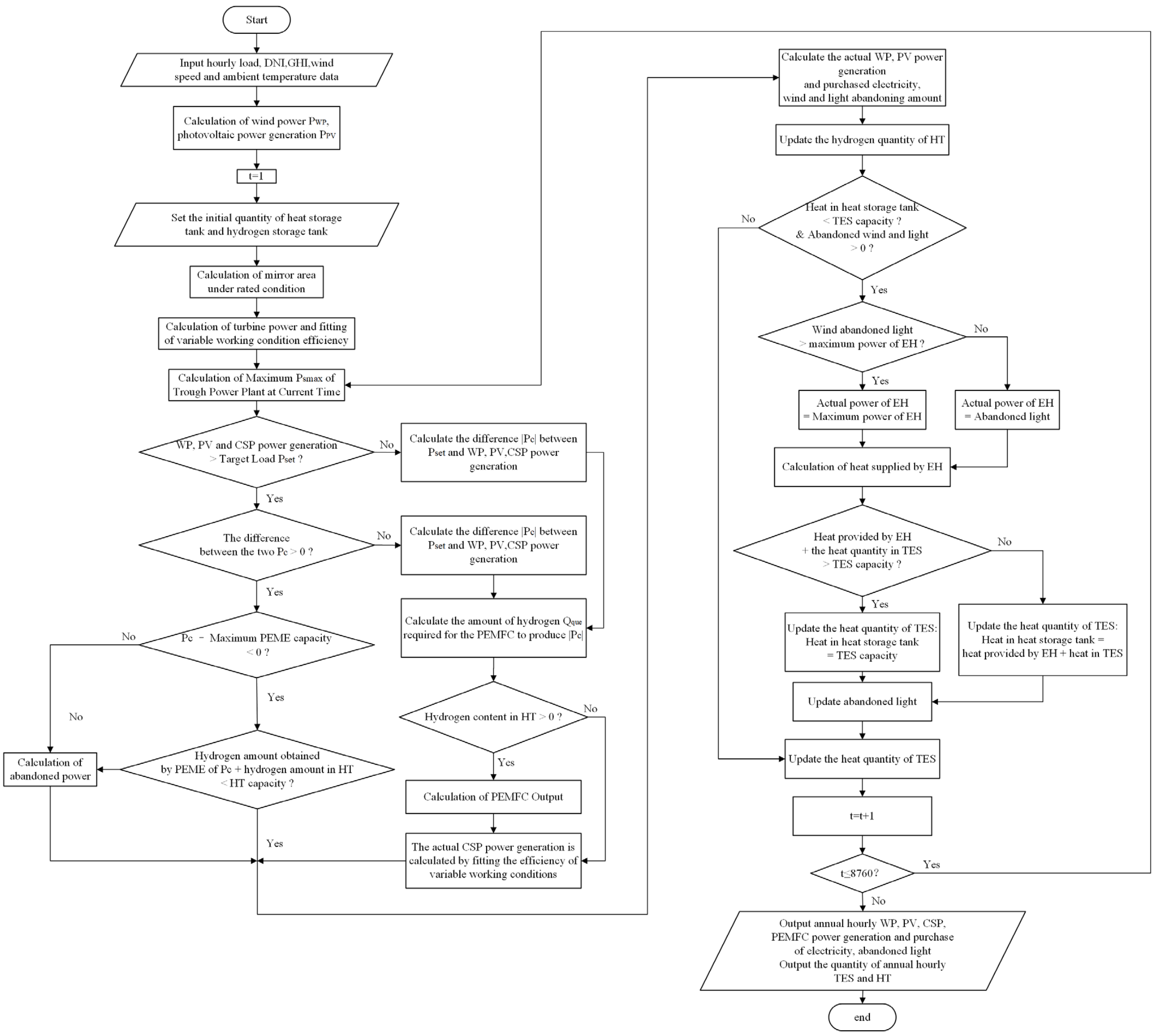

Figure 2. Operation strategy of the WSH-MES system.

When the PV and WP systems fall short in generating enough power to meet demand, a PEMFC becomes operational, supplying rapid peak power by using stored hydrogen from the hydrogen tank (HT). Further, if a deficit still exists after using the PEMFC, the CSP system contributes to balancing the energy equation. Only when all these systems are inadequate to meet the energy demands is power sourced from the governmental grid.

This operating strategy not only ensures that the renewable energy generated is used in the most efficient manner but also offers layered energy storage solutions. It accommodates storage limitations and provides a holistic response to the challenges of energy supply and demand. All these components and their interactions are visually represented in Figures 1 and 2 for a more intuitive understanding.

2.3. Model Construction and Validation

The mathematical model of PV, WP, CSP, PEME, HST, and PEMFC is introduced in Table 2. Among them, the CSP model includes an SF, TES, and a turbine.

Table 2. The modeling formula of the subsystem (Symbols as shown in Nomenclature).

Subsystem	Main Equations	Auxiliary Notes
PV	$P_{PV} = GHI \cdot n_m \cdot A_m \cdot \eta_{PV} \cdot \eta_{inv} \cdot f_{PV}$ $\eta_{PV} = \eta_{PV,NOM}[1 + \gamma(T_c - T_{c,ref})]$ $T_c = T_a + (T_{noct} - T_{a,noct})\frac{GHI}{GHI_{noct}}\frac{U_{L,noct}}{U_L}[1 - \frac{\eta_{PV}}{\tau \cdot \alpha}]$	Where effective area A_m and the quantity of PV panels n_m, the inverter's efficiency η_{inv}, and the derating factor f_{PV} are specified. Where T_c is the PV module's actual operating temperature; T_a is the surrounding air's temperature; T_{noct} is the nominal operating cell temperature; GHI_{noct} is the assumed level of global irradiation; $U_{L,noct}$ and U_L are heat transfer coefficients at the nominal and actual conditions, respectively; γ is the temperature coefficient, and $T_{c,ref}$ is the operating cell temperature under reference condition; η_{PV} is the actual PV efficiency; and $\tau \cdot \alpha$ is the transmittance–absorptance coefficient.
WP	$\frac{v_{70}}{v_{10}} = (\frac{h_{70}}{h_{10}})^k$ $P_w = \begin{cases} 0 & v_t < v_c \\ P_R^e(\frac{v_t - v_c}{v_r - v_c}) & v_c \le v_t \le v_r \\ P_R^e & v_r \le v_t \le v_f \\ 0 & v_t > v_f \end{cases}$	Where v_1 is the surface wind speed, m/s; v_2 is the wind speed at $h_2 = 70$ m from ground height, m/s; and k is the wind shear coefficient, $k = 0.14.v_c$ is the fan starting wind speed, m/s; v_r is the rated wind speed of fan, m/s; and v_f is the cut-off wind speed of fan, m/s. P_R^e is the rated output power of fan, MW; P_{WP} is the actual output power of fan, MW.
CSP	$Q_{SF} = (Q_{absorb} - Q_{loss} - Q_{pipe}) \cdot A \cdot 10^{-6}$ $\dot{Q}_{HTF} = \dot{m}_{HTF} \cdot (h_{out} - h_{in})$ $\eta_{red} = 0.191 - 0.409\frac{\dot{m}_{act}}{\dot{m}_{ref}} + 0.218(\frac{\dot{m}_{act}}{\dot{m}_{ref}})^2$ $\eta_{turb} = (1 - \eta_{red}) \cdot \eta_{ref}$	Where Q_{SF} is the heat gain power of heat-conducting oil in the SF, MW; Q_{absorb} is the solar heat absorbed with the collector tube, W/m^2; Q_{loss} is the heat loss of collector tube, W/m^2; Q_{pipe} is the pipe heat loss, W/m^2; and A is the area of SF, m^2. $\dot{m}_{HTF}$ is the mass flow of HTF; h_{in} and h_{out} are the specific enthalpies of the HTF inlet and outlet of the receiver, respectively. $\dot{m}_{act}$ is the actual mass flow of steam, $\dot{m}_{ref}$ is the reference mass flow of steam in design condition, η_{red} is the deviation proportion of steam turbine efficiency compared to that in design condition, and η_{ref} is the reference steam turbine efficiency in design condition. More detailed data can be found in [33].
PEME	$H_2O + electricity \rightarrow H_2 + \frac{1}{2}O_2$ $V = V_{ocv} + V_{act} + V_{diff} + V_{ohm}$	Where V_{ocv} is the theoretical minimum electrolytic voltage at which the electrolysis of water occurs; V_{act} is the open circuit voltage. V_{diff} is the equivalent overpotential due to diffusion, and V_{ohm} is the ohmic overpotential due to the proton exchange membrane. More detailed data can be found in [33].

Table 2. *Cont.*

Subsystem	Main Equations	Auxiliary Notes
HST	$E_{\text{HST}}(t) = E_{\text{HST}}(t-1) + \left(P_{\text{PEME-HST}}(t) - \frac{P_{\text{HST-FC}}(t)}{\eta_{\text{storage}}}\right) \times \Delta t$ $m_{\text{HST}}(t) = \frac{Q_{\text{HST}}(t)}{HHV_{H_2}}$	Where $P_{\text{HT-FC}}$ is the transferred power from the hydrogen tank to the FC. η_{storage} is the storage efficiency, and this efficiency is assumed to be 95% due to the loss incurred in transportation or storage. Where the Higher Heating Value (HHV) of hydrogen HHV_{H_2} is equal to 39.7 kWh/kg.
PEMFC	$H_2 + \frac{1}{2}O_2 \rightarrow H_2O + electricity$ $V = V_{\text{nernst}} - V_{\text{ohm}} - V_{\text{act}} - V_{\text{con}}$	Where V_{nernst} is the Nernst voltage, V_{ohm} is the ohmic overvoltage, V_{act} is the activation overvoltage, and V_{con} is the concentration overvoltage. More detailed data can be found in [33].

The WSH-MES system underwent rigorous simulation through Matlab/Simulink, based on the SF model validated in earlier studies [35]. To corroborate the model's precision, a comprehensive validation was undertaken, juxtaposing calculated and actual collector outlet oil temperatures across six distinct operating points by comparing it with experimental data from [38]. The detailed results are incorporated into Table 3, which reveal a deviation of less than 1%, confirming that the model satisfies the requisite accuracy benchmarks.

Table 3. Model validation of a solar field.

Test Conditions	DNI	Wind Speed	Ambient Temperature	Flow	Inlet Oil Temperature	Experimentally Measured Outlet Oil Temperature	Calculation Results	Error
	W/m^2	m/s	°C	L/min	°C	°C	°C	%
1	933.7	2.6	21.2	47.7	102.2	124.0	123.39	0.49
2	968.2	3.7	22.4	47.8	151.0	173.3	172.24	0.61
3	982.3	2.5	24.3	49.1	197.5	219.5	217.41	0.95
4	909.5	3.3	26.2	54.7	250.7	269.4	266.92	0.92
5	937.9	1.0	28.8	55.5	297.8	316.9	314.08	0.89
6	880.6	2.9	27.5	55.8	299.0	317.2	314.17	0.96

3. Bi-Level Capacity-Operation Collaborative Optimization Method

This study outlines a dual-layered optimization model that collaboratively works on both capacity and operation within the WSH-MES system, as shown in Figure 3. The model's higher level tackles a complex optimization issue, weighing both economic considerations and carbon emission factors in determining capacity distribution. Conversely, the model's lower level is dedicated to enhancing renewable energy usage by fine-tuning the scheduling of operational activities.

The general expression of the model is as follows:

$$\begin{array}{ll} \min\limits_{R_i}\{F_1(R_i, f), F_2(R_i, f)\} & \text{(1a)} \\ \max\limits_{H_i^t} f\left(R_i, H_i^t\right) & \text{(1b)} \\ s.t.\ \ g_0\left(R_i, H_i^t\right) \leq 0 & \text{(1c)} \end{array} \quad (1)$$

Equation (1) shows the two-level model consisting of capacity allocation optimization in the upper layer (Equation (1a)) and operation scheduling optimization in the lower layer (Equation (1b,c)). The upper-level optimization problem has two objective functions, F_1 and F_2, and the lower-level optimization problem has H_i as decision variables, which includes annual hourly energy generation for WP, PV, CSP, EH, TES charging/discharging, PEME, HST charging/discharging, and PEMFC. The lower-level optimization problem

g_0 has constraints on system output and power balance, and the objective function is f to maximize annual operation revenue.

To optimize the operation scheduling, a linearized full working condition model is constructed due to the huge scale of decision variables and the hourly basis (8760 h) for the system power output and charging/discharging power of heat and hydrogen storage systems. The linear programming method is used for the operation scheduling optimization. This section describes the objective function, lower-level constraints, and solution methods of the bi-level optimization model. The relevant technical parameters, computational time, and performance are shown in Table A1 in Appendix A.

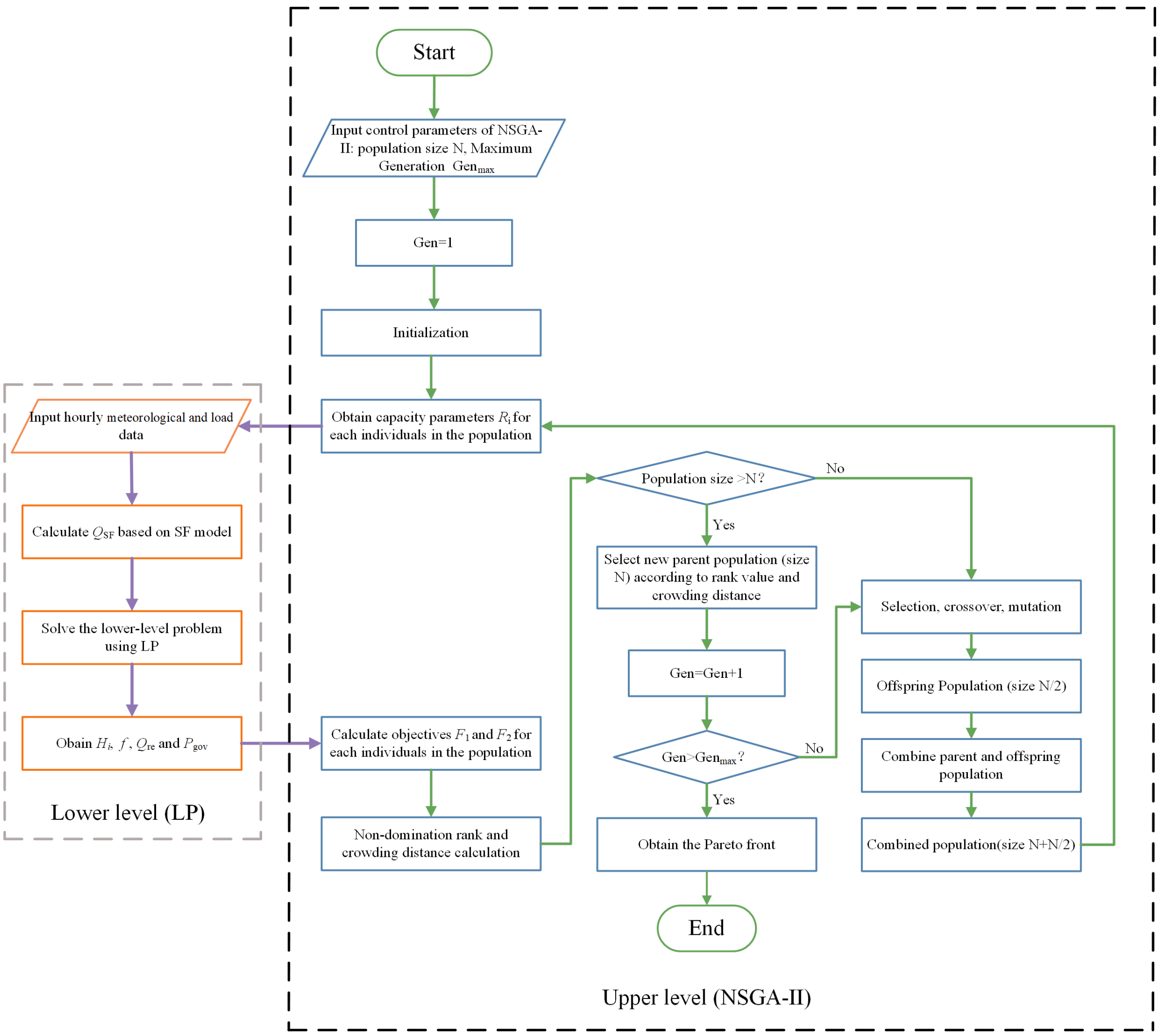

Figure 3. Flow chart of the algorithm for the bi-level optimization problem.

3.1. Source-Load Uncertainty Treatment

In order to fully take into account the source load uncertainty during the actual operation of the WSH-MES system, meteorological data and user load data based on long- and short-term memory network (LSTM) forecasts are used as inputs to the system. As LSTM can solve the problem of medium- and long-term time series forecasting [39], it has been widely used for time series forecasting, e.g., in the energy sector [40,41].

As shown in Figure 4, the connection of LSTM network modules is a chain structure, where the state of the cell C_t is the key to LSTM. It consists of three gates (forgetting gate f_t, input gate i_t, and output gate o_t) and internal memory state C_t. The main calculation process can be found in reference [42].

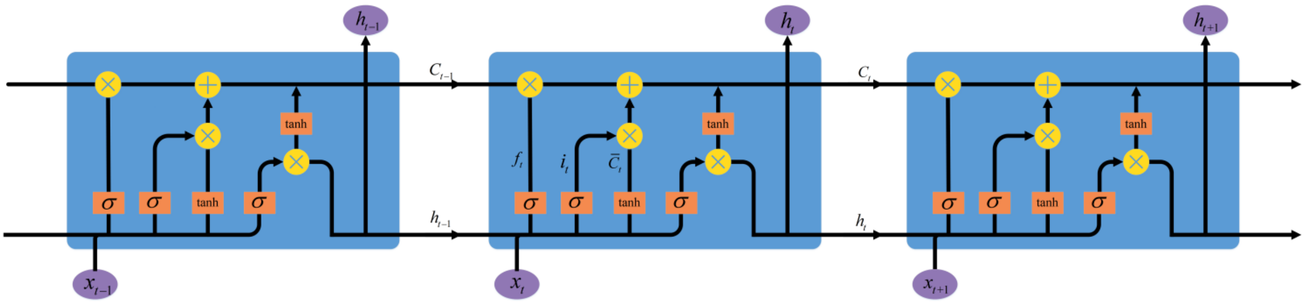

Figure 4. Internal unit structure of LSTM.

3.2. Objective Function

3.2.1. Lower-Level Objectives

The goal for the secondary level of optimization is to maximize the rate of renewable energy consumption. This research defines the primary renewable energy rate (PRER) as the target function for this lower-tier optimization model [36]. The intention is to minimize wasted wind and solar energy by devising a suitable operational strategy (detailed in Section 2.2). This approach aims to utilize as much renewable energy as feasible for either power generation or energy storage.

$$PRER = \frac{E_{useful}}{E_{tot}} = \frac{\sum\limits_{t=1}^{8760} (P_{\mathrm{PV}}^{\mathrm{user}}(t) + P_{\mathrm{WP}}^{\mathrm{user}}(t) + P_{\mathrm{CSP}}^{\mathrm{user}}(t) + P_{\mathrm{PEMFC}}^{\mathrm{user}}(t) + Q_{\mathrm{H_2}}^{\mathrm{user}}(t)) + Q_{\mathrm{HST}}^{\mathrm{rest}}(8760) + Q_{\mathrm{TES}}^{\mathrm{rest}}(8760)}{\sum\limits_{t=1}^{8760} (E_{\mathrm{wind}}^{\mathrm{power}}(t) + E_{\mathrm{solar}}^{\mathrm{power}}(t))} \tag{2}$$

PRER is defined as the output E_{useful} of the system to the renewable energy input E_{tot} to the system. Among them, $P_{\mathrm{WP}}^{\mathrm{user}}(t)$, $P_{\mathrm{PV}}^{\mathrm{user}}(t)$, $P_{\mathrm{CSP}}^{\mathrm{user}}(t)$, and $P_{\mathrm{PEMFC}}^{\mathrm{user}}(t)$ are the electricity directly supplied to the user with WP, PV, CSP, and PEMFC, respectively. $Q_{\mathrm{H_2}}^{\mathrm{user}}(t)$ is the hydrogen energy output. $Q_{\mathrm{HES}}^{\mathrm{rest}}(8760)$ and $Q_{\mathrm{TES}}^{\mathrm{rest}}(8760)$ are rest energy in HES and TES, separately. $E_{\mathrm{wind}}^{\mathrm{power}}(t)$ and $E_{\mathrm{solar}}^{\mathrm{power}}(t)$ are the wind and solar radiation resources, respectively.

This research aims to plan the system's yearly hourly power output, employing the LP technique for the secondary model's resolution. The final solution's parameters encompass LCOE and $E_{\mathrm{CO_2}}$. It is essential to establish boundaries for the secondary model, factoring in the power, TES system, and other modules, to guarantee that the system's scheduling remains within a logical scope. A detailed constraint model can be found in reference [37].

3.2.2. Upper-Level Objectives

The top-tier optimization, focusing on capacity distribution, grapples with a multi-objective challenge that seeks a balance between the financial aspects of the WSH-MES system and CO_2 emissions. The target function encompasses both the LCOE and CO_2 emissions.

(1) LCOE

LCOE serves as a unique measure for assessing the overall expense of generating electricity throughout the entire life cycle of a system.

$$LCOE = \frac{IC + \sum\limits_{\mathrm{n}=1}^{\mathrm{N}} \frac{C_{\mathrm{OM}}(n)}{(1+i)^n}}{\sum\limits_{n=1}^{N} \frac{P_{\mathrm{WP}}(n)\cdot(1-d_{\mathrm{WP}})^{n-1} + P_{\mathrm{PV}}(n)\cdot(1-d_{\mathrm{PV}})^{n-1} + P_{\mathrm{CSP}}(n)\cdot(1-d_{\mathrm{CSP}})^{n-1}}{(1+i)^n}} \tag{3}$$

In the given expression for LCOE, the numerator primarily focuses on the computation of investment and operation and maintenance (O&M) costs. Here, *IC* symbolizes the initial investment costs for the system under study, C_{OM} stands for the system's yearly O&M costs, and i signifies the discount rate, selected as 0.05 for this research. Additionally, n refers to the operating cycle, N represents the system's expected lifespan (set at 25 years in this study), and d indicates the annual degradation factor for each subsystem. The denominator mainly accounts for the system's power generation, where P_{WP}, P_{PV}, and P_{CSP} correspond to the generation power of WP, PV, and CSP (in MWh), respectively. Further details on the key economic parameters of the WSH-MES system can be found in reference [37].

(2) CO_2 emissions

When the energy produced with the WSH-MES system falls short of meeting user demand, additional power will be sourced from the grid. Notably, coal-powered generation remains a dominant contributor to grid power. Given that this study incorporates the CO_2 emissions from such sources, the optimization goal is to minimize the CO_2 emissions associated with power purchases. The computation for CO_2 emissions is detailed as follows, based on reference [33]:

$$E_{CO_2} = B_{s,sum} \cdot c_{ef} \tag{4}$$

$$B_{s,sum} = P_{purchase} \cdot b_s \tag{5}$$

In the provided equation, E_{CO_2} stands for the amount of CO_2 emissions in tons (t). $B_{s,sum}$ represents the yearly consumption of standard coal (t). The term c_{ef} is used to denote the CO_2 emission coefficient, with a value of 2.78 as referenced in study [33]. The variable $B_{s,sum}$ is determined with the system's yearly power acquisition $P_{purchase}$ (measured in MWh) and the coal consumption for each unit of b_s, kWh (t). In the context of this research, it is assessed that generating 1 kWh of electricity consumes 302 g of standard coal.

3.3. Solving Algorithm

In this research, a composite algorithm is presented, integrating both NSGA-II and LP methodologies, fortified with an elite strategy. This approach targets the bi-level capacity-operation collaborative optimization framework. The NSGA-II technique is designated for the primary multi-objective capacity arrangement optimization, while the LP approach focuses on the subsequent operation scheduling optimization. The workings of this bi-level optimization approach are graphically depicted in Figure 3. The methodology to navigate through this bi-level optimization framework is as follows:

Step 1: Set the operational parameters for the NSGA-II algorithm. This includes determining the population size, denoted as N, and the ceiling for iterations, termed Gen_{max}. In the context of this research, values of 300 for N and 80 for Gen_{max} were chosen to ensure a balance between the speed of convergence and the efficacy of the algorithm.

Step 2: Commence with an initial population setting of Gen = 1. Based on the site-specific conditions (referenced in Table 4), the optimization boundaries for the primary decision variables are set. These variables encompass loop count or SF size (x_1), CSP capacity (x_2), TES capacity (x_3), PV capacity (x_4), WT count or WF capacity (x_5), PEME capacity (x_6), HST capacity (x_7), and PEMFC capacity (x_8); N integer arrays R_i ([$x_{i,1}$, $x_{i,2}$, $x_{i,3}$, $x_{i,4}$, $x_{i,5}$, $x_{i,6}$, $x_{i,7}$, $x_{i,8}$) (with i ranging from 1 to N) are randomly selected to form the foundational population for the NSGA-II algorithm.

Step 3: Integrate the capacity distribution parameters R_i derived from the population into the secondary optimization model. The application of the linear programming methodology becomes pivotal in addressing this secondary model, seamlessly merging time-sequenced meteorological data with load and wind energy statistical insights.

Step 4: The computation shifts towards determining both the LCOE and CO_2 emissions for each individual within the population. This involves the utilization of Equations (3) and (4). Subsequently, non-dominance ranking and crowding computations are executed, harnessing the computed outcomes to establish rank values and crowding extents for every member.

Step 5: The current population count is scrutinized. Should this count align with N, the progression moves to Step 6. However, in case of a mismatch, the advancement transitions to Step 7.

Step 6: Generate an offspring population half the size of N. This population size is halved from N and is realized through a combination of selection processes, crossover, and mutation techniques. The amalgamation of this offspring cohort with the original population gives rise to a merged assembly, boasting a total size of 1.5 N. At this point, the loop is directed back to Step 3.

Step 7: N members are meticulously chosen based on their ranking and crowding metrics. These selected individuals lay the foundation for the forthcoming generation. An important conditional assessment takes place: if the generation count (Gen) surpasses a predefined threshold (Gen_{max}), the optimization procedure draws to a close, culminating in the display of the Pareto front. Alternatively, if Gen remains within the prescribed limit, its value is incremented by one, and the cycle reverts back to Step 6.

Table 4. Optimization interval of capacity parameters.

Parameter	Unit	Range
x_1	-	[0–776]
x_2	MW	[0–150]
x_3	h	[0–20]
x_4	MW	[0–150]
x_5	-	[0–66]
x_6	MW	[0–50]
x_7	m^3	[0–10]
x_8	MW	[0–50]

4. Case Study

This section uses a case study based on a WSH-MES system to apply the suggested optimization approach and demonstrate the feasibility of the bi-level capacity-operation collaborative optimization model.

4.1. Basic Parameters

The WSH-MES system, located in Zhangbei (41.2° N, 114.7° E), was subject to an exhaustive analysis to optimize its key equipment capacity and its hourly operation across the year. The optimization targeted a range of capacity parameters, encompassing the size of the SF, and the capacities of CSP, TES, PV, WP, PEME, HST, and PEMFC.

The LSTM model adopts a single hidden layer structure, and the node number of the hidden layer is 50. The Adam method is applied in training of the LSTM model, and the batch size is set as 64. The dropout is set as 0.1 to avoid overfitting. The last year data were used as the test set and the previous data were divided into training and validation sets. The validation set was used to evaluate the generalization performance of the model. The training set was used to train the LSTM model. The training curve of DNI is shown in Figure 5. The trained LSTM model is predicted on the training set and validation set, respectively. The training set and validation set errors are shown in Table 5. From the results in the table, it can be seen that the validation set error of each parameter is slightly lower than the training set error except for DHI, and the validation set error of DHI is also close to the training set error. It indicates that the prediction model constructed by using the LSTM algorithm has no overfitting phenomenon.

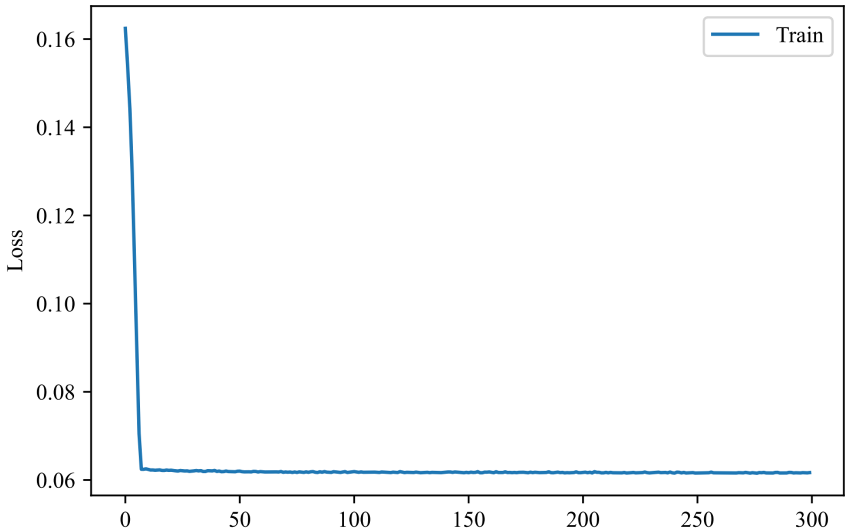

Figure 5. Training curve for the DNI prediction model.

Table 5. Training and validation set errors.

Dataset	RMSE (Training Set)	RMSE (Validation Set)
DNI (W/m^2)	191.84	199.29
GHI (W/m^2)	116.69	95.14
Wind speed (m/s)	1.55	1.38
Temperature (°C)	1.50	1.41

Figures 6 and 7 present the original and predicted meteorological and load data, respectively. For detailed equipment parameters and cost-related information, please refer to reference [36].

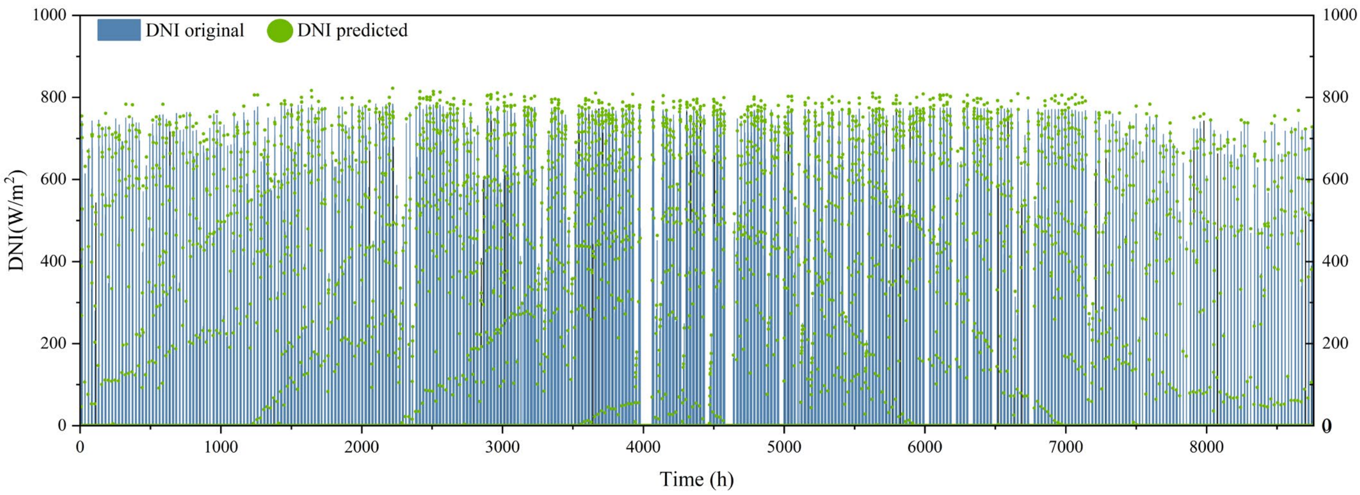

(**a**) Original DNI and predicted DNI.

Figure 6. *Cont.*

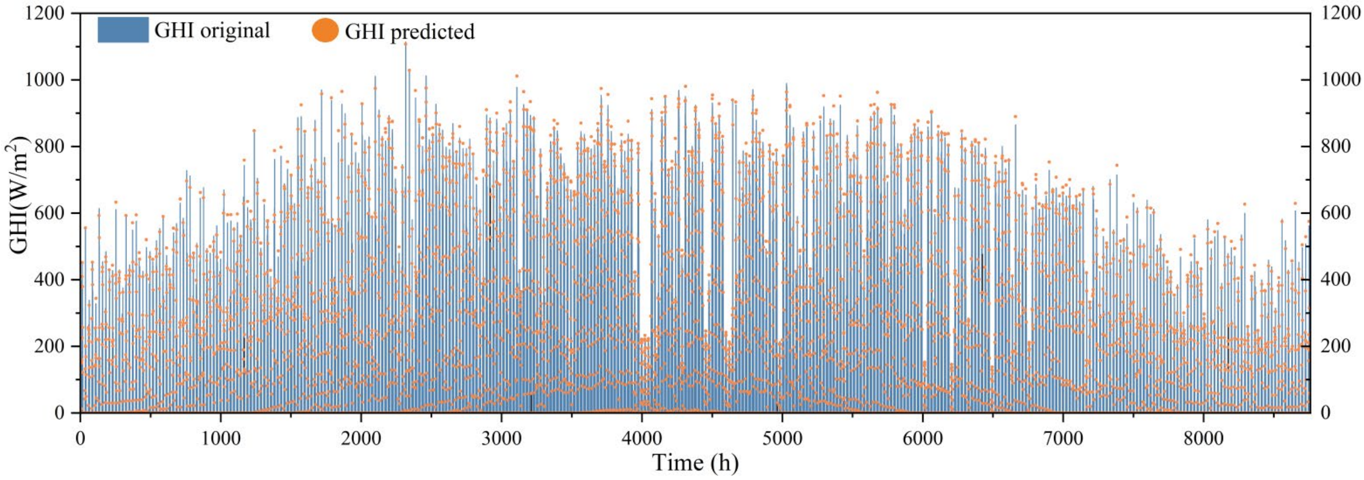

(**b**) Original GHI and predicted GHI.

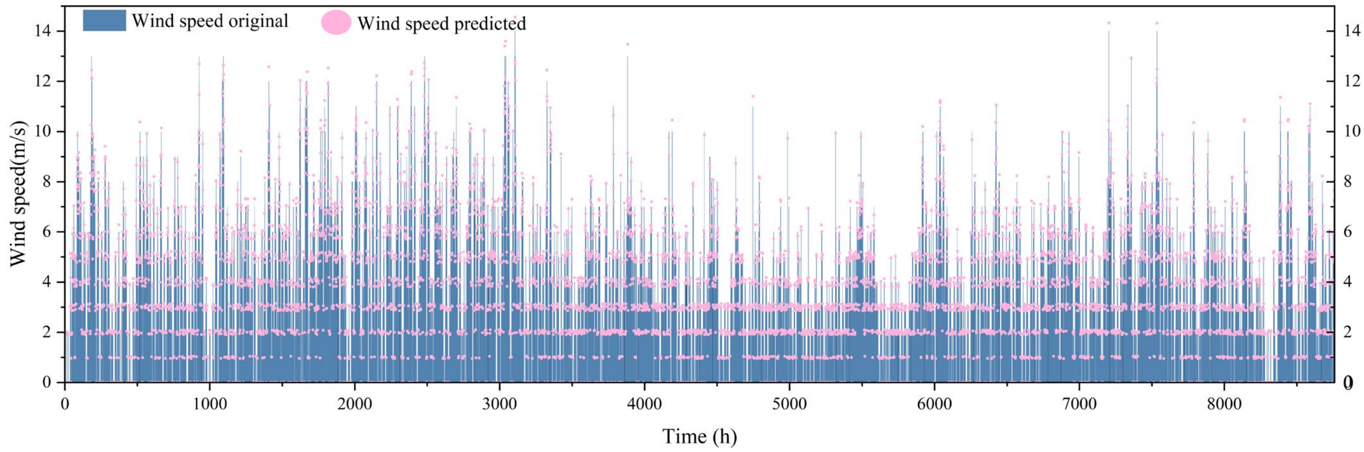

(**c**) Original wind speed and predicted wind speed.

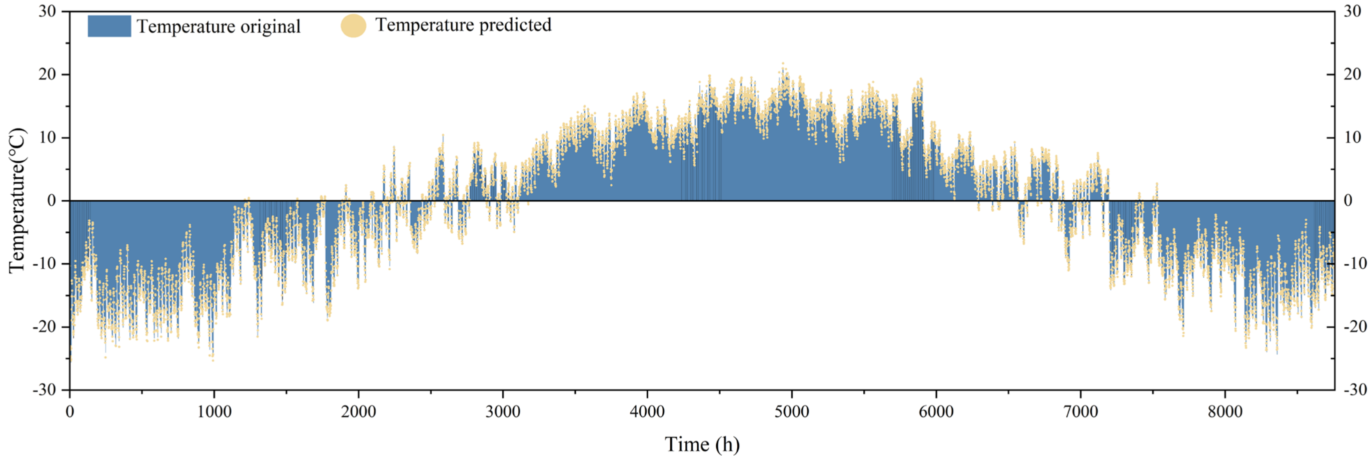

Figure 6. The original and predicted values of hourly weather date [33,43].

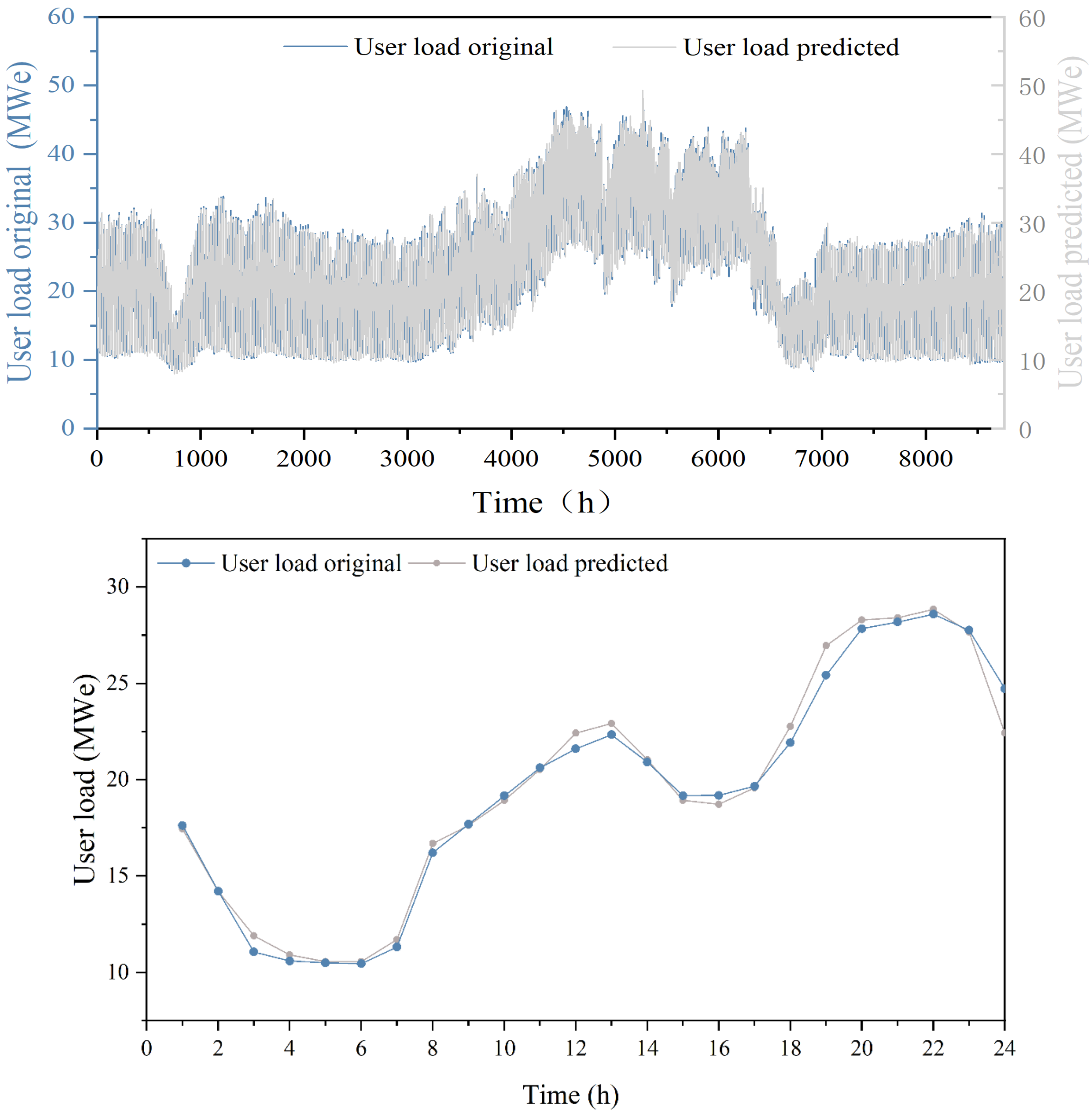

Figure 7. The original and predicted values of user load.

To reflect the prediction performance of the LSTM model, a Persistence model is used for a comparative analysis. The results are shown in Table 6. The results show that the error of the LSTM model is significantly lower than the Persistence model, indicating that the prediction performance of the LSTM model for each parameter is significantly better than the Persistence model.

Table 6. Prediction model performance evaluation.

Model	DNI (W/m^2)		GHI (W/m^2)		Wind Speed (m/s)		Temperature (°C)	
	RMSE	MAE	RMSE	MAE	RMSE	MAE	RMSE	MAE
LSTM	178.22	82.78	97.07	49.39	1.39	0.98	0.88	0.61
Persistence	199.62	87.53	105.31	60.23	1.42	1.00	1.02	0.74

4.2. Pareto Front

The optimization method proposed in this study utilizes the predicted annual hourly load and weather to optimize the capacity and operating schedule of the critical equipment in the WSH-MES system. The convergence stage of the optimization process is depicted in Figure 8.

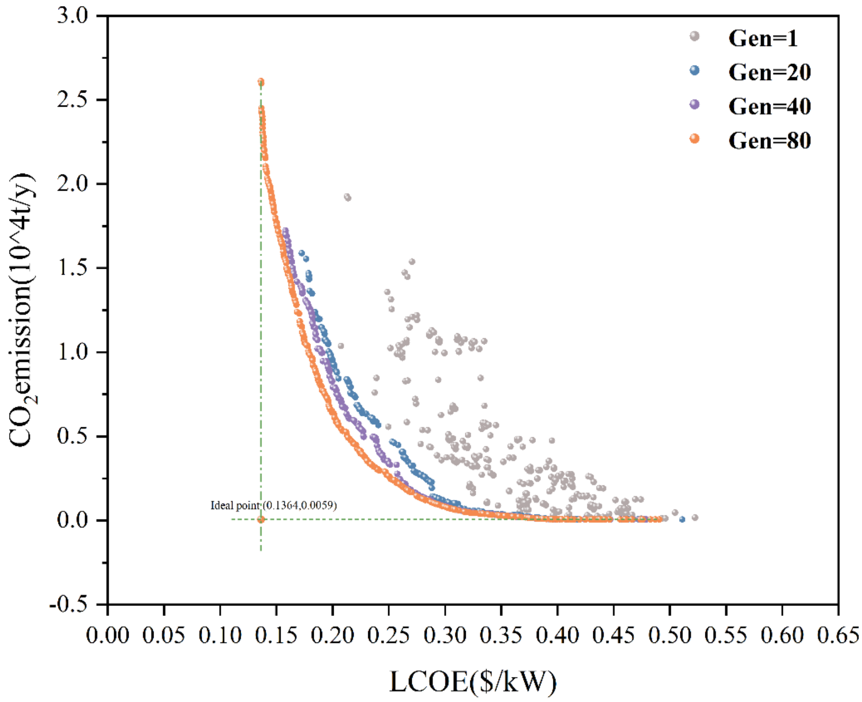

Figure 8. The convergence process of the optimization algorithm.

As illustrated in Figure 8, the Pareto front curve for this optimization problem (represented with the orange curve in the figure) is achieved after 80 generations of optimization. The rightmost point on this Pareto front curve is (3.26, 0.0059), which indicates the optimal capacity allocation point that minimizes the CO_2 emissions of the WSH-MES system.

The corresponding capacity configurations are 776 loops, 96 MW CSP capacity, 19 h TES capacity, 150 MW PV capacity, 66 WT, 37 MW PEME capacity, 9.024 m^3 HST capacity, and 27 MW PEMFC capacity. All six capacity parameters fall within their corresponding optimization interval, but three parameters (SF size, PV capacity, and WF capacity) are on the boundary of the optimization interval. These three variables determine the amount of energy input into the system, and in order to meet the user load as much as possible, it is necessary to increase the energy input to the system as much as possible. Consequently, to minimize the power purchase from the grid, the optimized installed capacity is larger than the actual local installed capacity. Therefore, there exists a relative optimal capacity allocation point within the optimization constraint interval for CO_2 emissions.

Regarding the economic index, the corresponding optimal capacity allocation point for the economic index is the leftmost point of the Pareto front curve, which is (0.1364, 2.6113). The corresponding capacity configurations for this point are 165 loops, 13 MW CSP capacity, 13 h TES capacity, 13 MW PV capacity, 13 WT, 0 MW PEME capacity, 0 m^3 HST capacity, and 0 MW PEMFC capacity. Four of these capacity allocations are located on the boundary, while the installed capacity of PV and WP is also lower. This is because the SF and hydrogen energy network (PEME, HST, and PEMFC) have high costs, and with lower renewable energy generation, the average energy cost is lower. Therefore, there is no corresponding optimal capacity configuration for economic indicators.

4.3. Best Compromise Solution Selection

Upon completing the optimization computations, several Pareto front solutions emerged, each reflecting distinct system performance characteristics. To pinpoint the most practical compromise solution, additional constraints were necessary. The most effective approach typically involves employing decision-making techniques to extract the optimal solution. In this context, a novel evaluation method was crafted, leveraging a comprehensive evaluation approach that combines the AHP-entropy assignment method and TOPSIS. The Pareto optimal solution, derived through this method, was selected as the final best solution after evaluating each index. The evaluation results under different weights are shown in Table 7.

Table 7. Pareto optimal scheme for LCOE and CO_2 emission with different solutions.

Weight	N_{loops} (-)	C_{CSP} (MW)	C_{TES} (h)	C_{PV} (MW)	N_{WT} (-)	C_{PEME} (MW)	V_{HST} (m^3)	C_{PEMFC} (MW)	LCOE (USD/kW)	CO_2 Emission ($\times 10^4$ t/y)
[0.32, 0.68]	424	44	20	88	36	5	2.914	2	0.251	0.245
[0.24, 0.76]	424	44	20	113	46	9	6.392	4	0.275	0.147
[0.19, 0.81]	424	45	20	122	45	9	6.016	4	0.2795	0.133
[0.16, 0.84]	456	48	20	121	48	11	7.05	5	0.2916	0.098
[0.10, 0.90]	456	55	20	133	51	10	7.144	5	0.3066	0.07

The optimal compromise results in an LCOE of 0.3096 USD/kW and CO_2 emissions of 630 t/y. The N_{loops}, CSP capacity, TES capacity, PV capacity, N_{WT}, PEME capacity, HST capacity, and PEMFC capacity for this treatment are 456, 55 MW, 20 h, 133 MW, 51, 10 MW, 7.144 m^3, and 5 MW, respectively. The economic analysis demonstrates that a 1% reduction in site CO_2 emissions corresponds to a 1.7% increase in the system's LCOE.

4.4. Analysis of Annual Operation Performance

The optimal point on the Pareto front is achieved through hourly heat and power load dispatch and appropriate capacity configuration in the WSH-MES system. Figure 8 depicts the daily output of the system for the best compromise solution.

As depicted in Figure 9, the optimized WSH-MES system is capable of meeting the electrical load demands, with 98.6% of the electricity generated from renewable sources. Furthermore, the system also provides access to hot water for users.

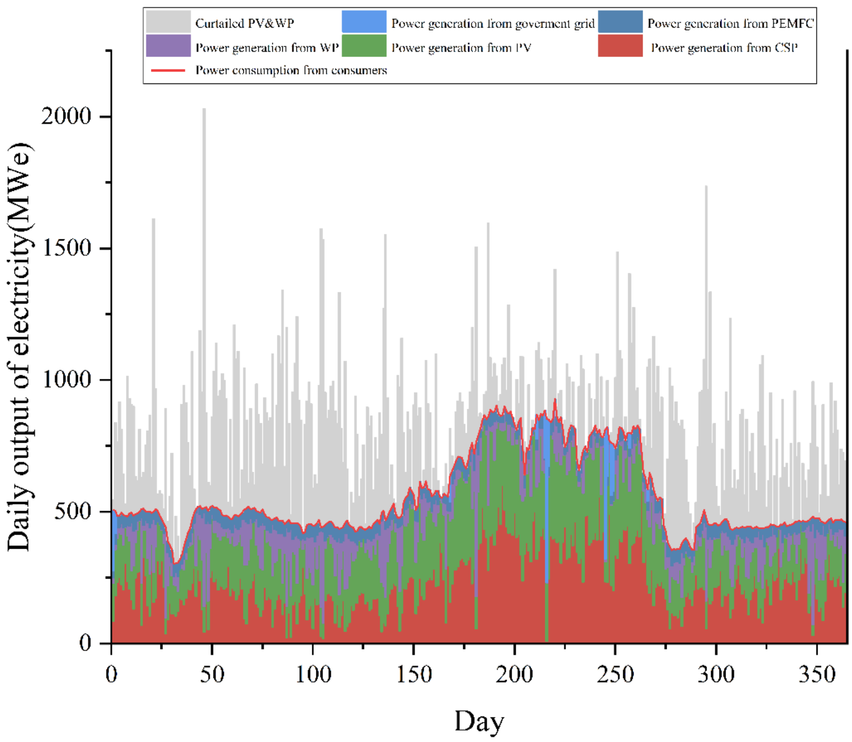

(**a**) Electricity.

Figure 9. *Cont.*

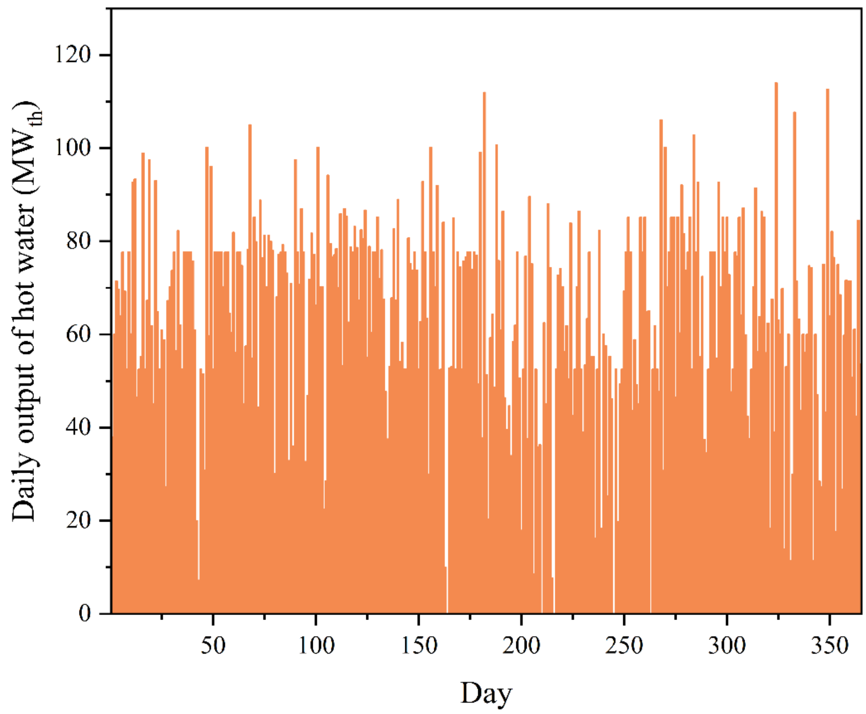

(**b**) Heat.

Figure 9. Daily output of the WSH-MES system in a typical year.

5. Sensitivity Analysis

The analysis examines the impact of SF size, CSP capacity, TES capacity, PV capacity, WP capacity, PEME capacity, HST capacity, and PEMFC capacity on the LCOE and CO_2 emissions of the system, highlighting the significance of capacity parameters in affecting these outcomes.

Figure 10 presents the variation of system LCOE and CO_2 emission when the SF size changes. As the figure shows, the LCOE decreases initially and then increases as the SF size increases. This trend results from the low system investment associated with small SF sizes. As the SF size grows, the system investment gradually increases, leading to a corresponding rise in the LCOE. However, if the SF size is too small, the heat input to the CSP is also too low, resulting in a reduction in the system output. Therefore, environmental impact considerations should also be taken into account when selecting the SF size. In terms of environmental benefits, CO_2 emissions continue to decrease as the SF size increases, due to the improved peaking ability of the system as more heat is collected with the SF, leading to higher CSP output. However, because the TES capacity is fixed, the heat in TES cannot be increased limitlessly with larger loops, ultimately resulting in CO_2 emissions flattening out.

As shown in Figure 11, the LCOE of the system decreases and then increases as the CSP increases. Because when the CSP capacity is less than 20 MW, the power generation of CSP increases with the increase in CSP capacity. However, when the CSP capacity exceeds 20 MW, the increase in system investment exceeds the increase in system power generation, resulting in a gradual increase in the LCOE of the system. When the CSP capacity reaches 77 MW, the LCOE of the system is the same as the initial LCOE, indicating that the CSP capacity is suitable from 0 to 77 MW, and an appropriate increase in CSP capacity can improve the peaking response capability of the system. Moreover, as the CSP capacity increases, the CO_2 emissions gradually decrease and eventually level off. This is because the TES and SF sizes of the system are fixed, and increasing the CSP capacity does not increase the CSP power generation. Therefore, the CO_2 emissions will level off after reaching the limit.

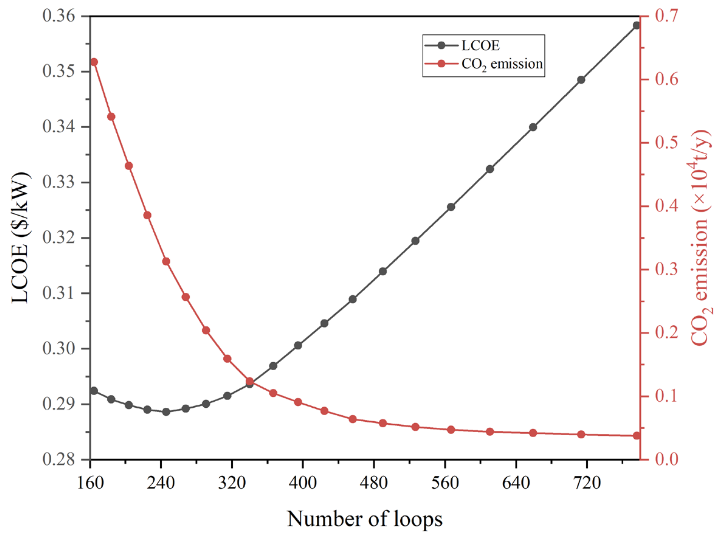

Figure 10. LCOE and CO_2 emission of WSH-MES system with different SF size.

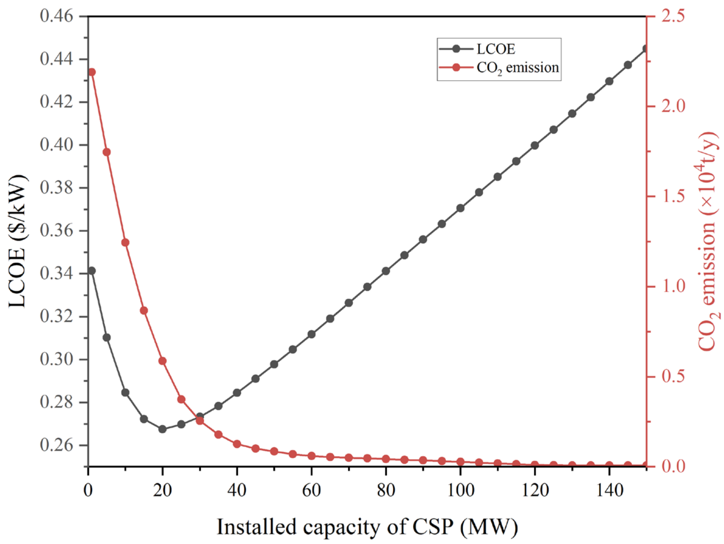

Figure 11. LCOE and CO_2 emission of WSH-MES system with different CSP capacity.

As illustrated in Figure 12, the LCOE of the system initially decreases and then increases with the increase in TES capacity. When the TES capacity exceeds 8 h, the LCOE gradually increases due to the increased system investment, which surpasses the increase in system power generation. On the other hand, the CO_2 emissions of the system gradually decrease with the rise in TES capacity. Although the system LCOE experiences a slight increase after TES capacity exceeds 8 h, the system CO_2 emissions continue to decrease, indicating that increasing the TES capacity can enhance the system's operational performance. However, since the TES capacity has a limit, the TES capacity of 20 h is optimal for the system capacity configuration.

Figure 13 indicates the effect of installed PV capacity on the system performance. As depicted in the figure, the system LCOE decreases and then increases with the increase in PV capacity. When the PV capacity is 50 MW, the system has the best economy at this time. The CO_2 emissions of the system gradually decrease as the PV capacity increases because the system's power generation also increases correspondingly. However, it should be noted that excessive PV capacity can negatively impact the system economy, and the capacity of the PEME is fixed. Therefore, an excessively large PV capacity can exacerbate the system's abandonment phenomenon, resulting in unnecessary waste.

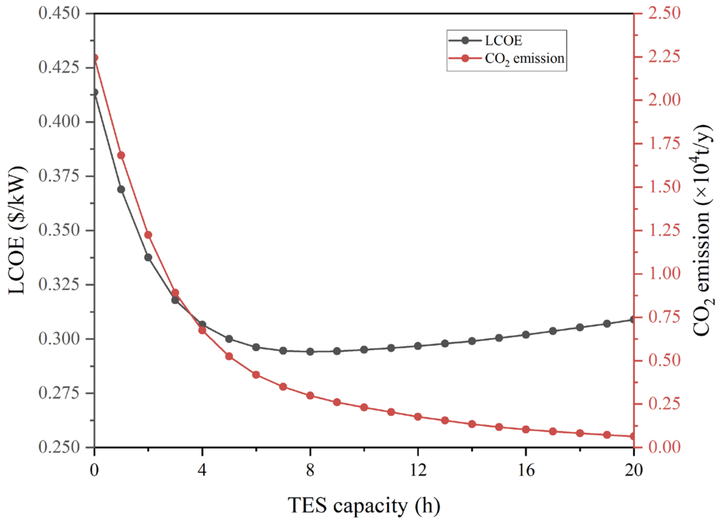

Figure 12. LCOE and CO_2 emission of WSH-MES system with different TES capacity.

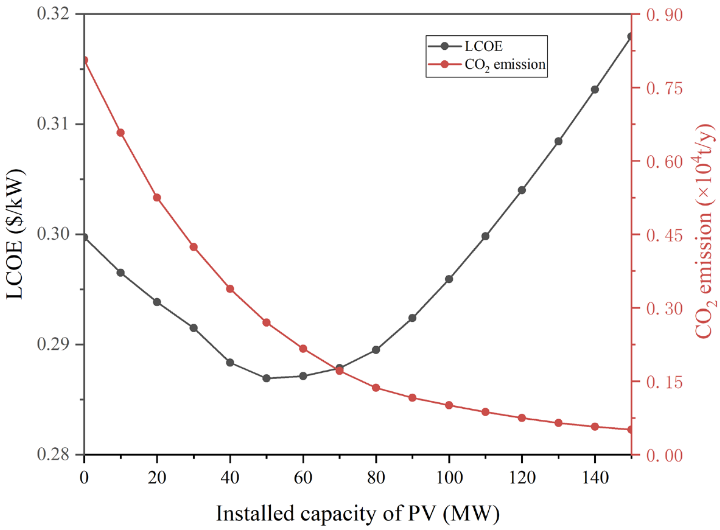

Figure 13. LCOE and CO_2 emission of WSH-MES system with different PV capacity.

As shown in Figure 14, the system's LCOE gradually increases as the number of WT increases. Because the increase in the number of WT leads to a significant increase in system investment. However, the CO_2 emissions decrease as the number of WT increases, as the power generation of the system increases to a certain extent. Combining Figure 13 with Figure 14, it becomes evident that wind farms can reduce CO_2 emissions by about 25% compared to PV. Since the installed capacity of WP is approximately half that of PV capacity, WP can complement PV by generating electricity at night. It plays the role of supplementing PV power generation during the day and CSP and PEMFC power generation at night, making it an effective power generation option.

As can be seen from Figure 15a, the LCOE of the WSH-MES system first decreases and then increases as the PEME capacity increases. Meanwhile, CO_2 emissions first decrease and then level off, with an optimal solution found at a capacity of around 10 MW. Because PEME plays a crucial role in consuming the electricity stored on an abandoned wind and solar basis, producing hydrogen energy, and compensating for user load deficits through PEMFC generation.

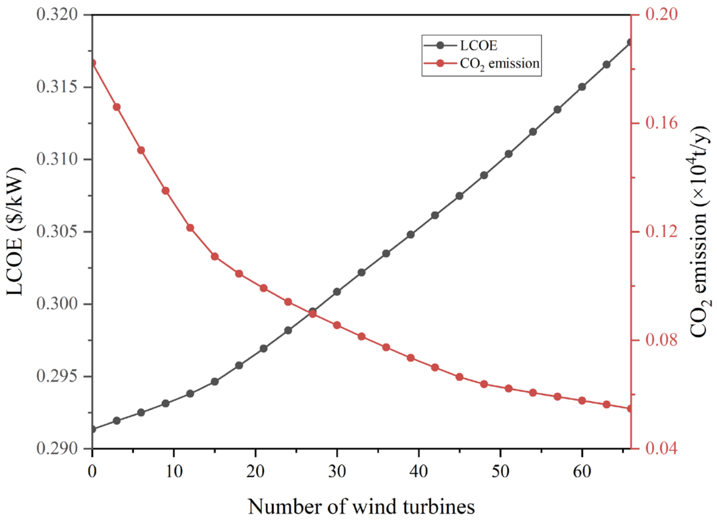

Figure 14. LCOE and CO_2 emission of WSH-MES system with different WP capacity.

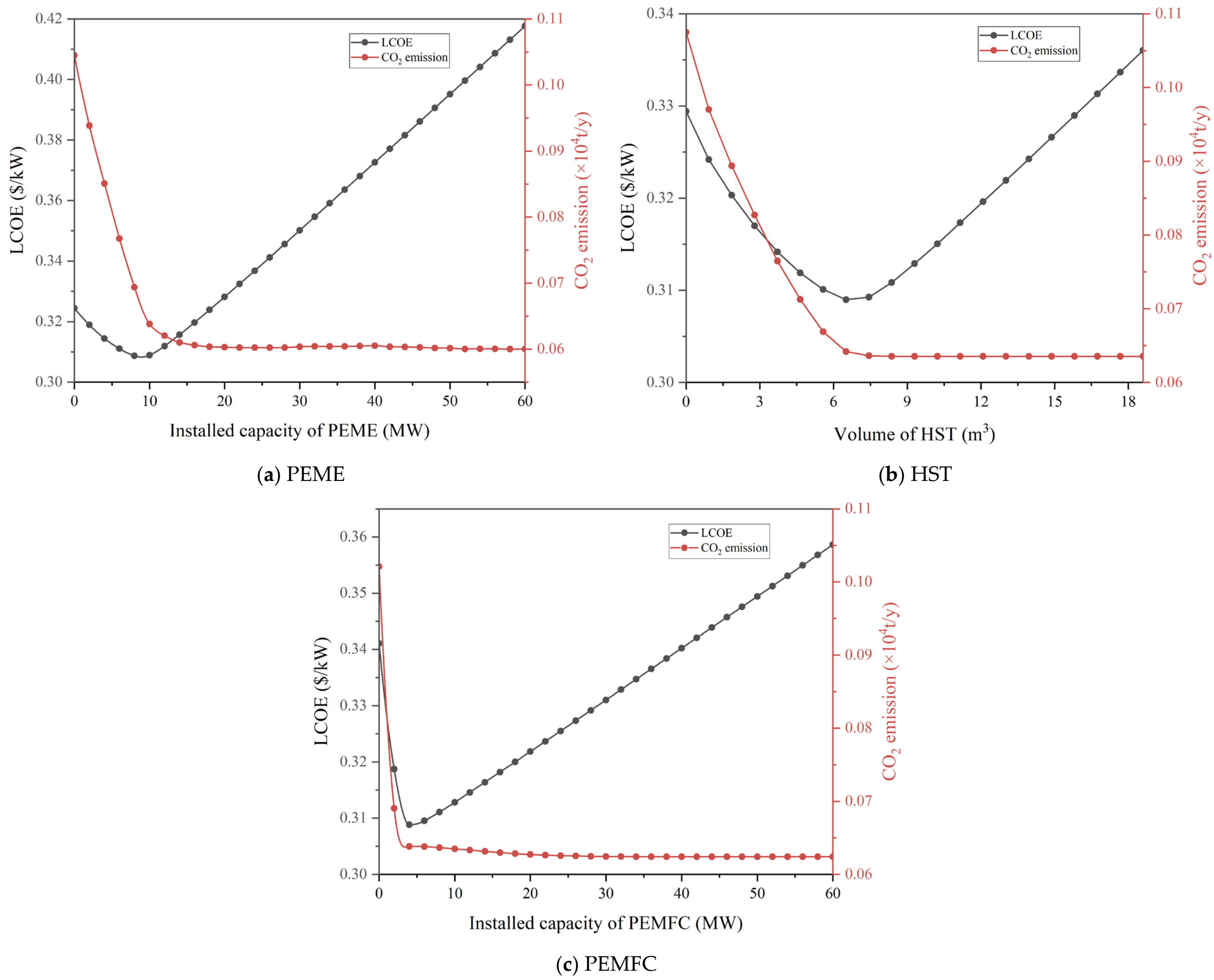

Figure 15. LCOE and CO_2 emission of WSH-MES system with different PEME, HST, and PEMFC capacity.

In Figure 15b, the trend of LCOE and CO_2 emissions variation with HST capacity is similar to that of PEME. HST mainly functions as a hydrogen energy storage to complement the PEME.

Figure 15c illustrates the change in system LCOE and CO_2 emissions as the PEMFC capacity varies. As shown in the figure, the LCOE first decreases and then increases with the increase in PEMFC capacity. Because as the PEMFC capacity increases, it acts as a peaking power source that can respond quickly, leading to an increase in power generation that exceeds the increase in system investment costs. However, as the PEMFC capacity continues to increase, the investment cost of the system will exceed the increase in power generation, resulting in a gradual increase in LCOE. Regarding environmental benefits, CO_2 emissions first decrease and then flatten out as PEMFC capacity increases. When the PEMFC capacity is small, the PEME can provide the hydrogen required by PEMFC, which enables system power generation to increase, but it is limited with the capacities of PEME and HST, which limits the hydrogen supplied to PEMFC. Beyond this range, the amount of hydrogen no longer increases, and the system power generation remains constant, resulting in no further change in CO_2 emissions. Under the current operation strategy, the overall trend in the change of PEME capacity, HST capacity, and PEMFC capacity is consistent, with a proportion of approximately 1:2:1.4.

6. Conclusions

This research introduces a WSH-MES system, integrating a wind farm, PV power station, CSP power station, and hydrogen energy network at the grid level for the co-generation of hydrogen and thermal energy. A sophisticated bi-level-capacity co-optimization model was formulated to concurrently optimize large-scale equipment capacity and annual load dispatch. To tackle this intricate bi-level optimization challenge, a nested algorithmic approach employing LP and the NSGA-II was deployed. The optimal compromise solution is also found using a combination of TOPSIS and AHP-entropy allocation methods.

Focusing on a WSH-MES system in Zhangbei, China, and incorporating uncertain weather data and electricity demand profiles, the proposed optimization strategy yielded a Pareto-optimal solution. This solution features an LCOE of USD 0.31/kW and CO_2 emissions of 630 t/y. Key parameters such as N_{loops}, CSP capacity, TES capacity, PV capacity, number of WT, PEME capacity, HST capacity, and PEMFC capacity were optimized to 456, 55 MW, 20 h, 133 MW, 51, 10 MW, 7.144 m^3, and 5 MW, respectively. The economic analysis revealed that each 1% reduction in CO_2 emissions led to a 1.7% increase in the system's LCOE, underscoring the economic trade-offs involved in carbon mitigation. The optimized WSH-MES system demonstrated substantial reductions in annual WP and PV curtailment, as well as CO_2 emissions, compared to a reference system. The sensitivity analysis indicated that the LCOE of the WSH-MES system exhibited a non-linear response to changes in various capacities, with PV installed capacity emerging as the most significant factor affecting maximum CO_2 emissions.

In future endeavors, the model and framework delineated in this paper will undergo refinements to incorporate dynamic energy flow characteristics, user behavior, stochastic distributed power output, and the influence of heat and hydrogen storage on system operation. These enhancements aim to bolster both the practical applicability and reliability of the study's conclusions.

Author Contributions: Conceptualization, L.L. and R.Z.; methodology, L.L. and Y.H.; software, L.L., Y.H. and Y.X.; validation, Y.H., Y.X. and C.S.; formal analysis, L.L. and Y.H.; investigation, L.L., Y.X. and C.S.; resources, R.Z.; data curation, Y.H.; writing—original draft preparation, L.L., Y.H. and Y.X.; writing—review and editing, R.Z.; visualization, L.L., Y.H., Y.X. and C.S.; supervision, R.Z.; project administration, H.Y. and Q.W.; funding acquisition, R.Z. All authors have read and agreed to the published version of the manuscript.

Funding: This research was funded by the National Natural Science Foundation of China grant number (No. 52090060). And The APC was funded by (No. 52090060).

Institutional Review Board Statement: Not applicable.

Informed Consent Statement: Not applicable.

Data Availability Statement: The data presented in this study are available on request from the corresponding author. The data are not publicly available due to privacy restriction.

Conflicts of Interest: The authors declare no conflict of interest.

Nomenclature

Nomenclature	
C	capacity
C_{OM}	operation and maintenance costs (USD)
E_{hw}	hot water heating produced with the PEMFC (MW_{th})
N	number
P_{CSP}	electric power generated from concentrated solar thermal power (MW_e)
P_{PEME}	the electric power that enters the proton exchange membrane electrolyzer (MW_e)
P_{PEMFC}	electric power generated from PEMFC (MW_e)
P_{gov}	purchased power (MW_e)
P_{load}	power load of consumers (MW_e)
P_{PV}	electric power generated from photovoltaics (MW_e)
P_{qi_WP}	abandoned wind power (MW_e)
P_{WP}	electric power generated from wind power (MW_e)
$\dot{Q}_{qi\_solar}$	thermal power abandoned by solar collector field (MW_{th})
$\dot{Q}_{SF}$	heating power of heat conducting oil in solar collector (MW_{th})
$\dot{Q}_{solar}$	the solar thermal power output with the heat storage system (MW_{th})
Q_{state}	the thermal power of heat storage system (MW_{th})
Q_{HST}	the energy of hydrogen stored in the hydrogen storage and transportation (MW)
T_a	ambient temperature (°C)
V	volume (m^3)
η_{PEME}	proton exchange membrane electrolyzer efficiency
$\eta_{storage}$	storage efficiency
η_{FC}	fuel cell efficiency

Superscript	
t	t-th hour
Abbreviations	
CSP	concentrated solar thermal power
DNI	direct normal irradiance
EH	electric heater
GHI	global horizontal irradiance
LSTM	Long Short-Term Memory Network
HST	hydrogen storage and transportation
HT	hydrogen tank
IC	initial investment
MES	multi-energy system
PEME	proton exchange membrane electrolyzer
PEMFC	proton exchange membrane fuel cell
PV	photovoltaic
SF	solar field
TES	thermal energy storage
WF	wind farm
WP	wind power
WSH-MES	wind-solar-hydrogen multi-energy supply
4E	energy, exergy, economy, and environmental

Appendix A

Table A1. Technical data and calculation time.

Parameter	Value
Average computation time of NSGA-II	5.5 h
Total computation time of NSGA-II	250 h
Computation time for reference case of NSGA-II	4.8 h
CPU and memory resources	Intel® I7-4790 4 Cores @3.60 GHz, 16 GB RAM
Operating system	Microsoft Windows 11 Enterprise
MATLAB® version	MATLAB® R2021a

References

1. Arent, D.J.; Green, P.; Abdullah, Z.; Barnes, T.; Bauer, S.; Bernstein, A.; Berry, D.; Berry, J.; Burrell, T.; Carpenter, B. Challenges and opportunities in decarbonizing the US energy system. *Renew. Sustain. Energy Rev.* **2022**, *169*, 112939. [CrossRef]
2. Malhan, P.; Mittal, M. A novel ensemble model for long-term forecasting of wind and hydro power generation. *Energy Convers. Manag.* **2022**, *251*, 114983. [CrossRef]
3. Notton, G.; Nivet, M.-L.; Voyant, C.; Paoli, C.; Darras, C.; Motte, F.; Fouilloy, A. Intermittent and stochastic character of renewable energy sources: Consequences, cost of intermittence and benefit of forecasting. *Renew. Sustain. Energy Rev.* **2018**, *87*, 96–105. [CrossRef]
4. Pater, S. Increasing Energy Self-Consumption in Residential Photovoltaic Systems with Heat Pumps in Poland. *Energies* **2023**, *16*, 4003. [CrossRef]
5. Pater, S. Field measurements and energy performance analysis of renewable energy source devices in a heating and cooling system in a residential building in southern Poland. *Energy Build.* **2019**, *199*, 115–125. [CrossRef]
6. Pousinho, H.M.I.; Esteves, J.; Mendes, V.M.F.; Collares-Pereira, M.; Cabrita, C.P. Bilevel approach to wind-CSP day-ahead scheduling with spinning reserve under controllable degree of trust. *Renew. Energy* **2016**, *85*, 917–927. [CrossRef]
7. Chennaif, M.; Zahboune, H.; Elhafyani, M.; Zouggar, S. Electric System Cascade Extended Analysis for optimal sizing of an autonomous hybrid CSP/PV/wind system with Battery Energy Storage System and thermal energy storage. *Energy* **2021**, *227*, 120444. [CrossRef]
8. Wahbah, M.; Mohandes, B.; EL-Fouly, T.H.M.; El Moursi, M.S. Unbiased cross-validation kernel density estimation for wind and PV probabilistic modelling. *Energy Convers. Manag.* **2022**, *266*, 115811. [CrossRef]
9. Yang, J.; Yang, Z.; Duan, Y. Load matching and techno-economic analysis of CSP plant with S-CO_2 Brayton cycle in CSP-PV-wind hybrid system. *Energy* **2021**, *223*, 120016. [CrossRef]
10. Ding, Z.; Hou, H.; Duan, L.; Huang, C.; Hu, E.; Yu, G.; Zhang, Y.; Zhang, N. Simulation study on a novel solar aided combined heat and power system for heat-power decoupling. *Energy* **2021**, *220*, 119689. [CrossRef]
11. Wang, Z.; Zhang, X.; Rezazadeh, A. Hydrogen fuel and electricity generation from a new hybrid energy system based on wind and solar energies and alkaline fuel cell. *Energy Rep.* **2021**, *7*, 2594–2604. [CrossRef]
12. Li, Z.; Hou, S.; Cao, X.; Qin, Y.; Wang, P.; Che, S.; Sun, H. Modeling and analysis of hydrogen storage wind and gas complementary power generation system. *Energy Explor. Exploit.* **2021**, *39*, 1306–1323. [CrossRef]
13. Al-Ghussain, L.; Ahmad, A.D.; Abubaker, A.M.; Hassan, M.A. Exploring the feasibility of green hydrogen production using excess energy from a country-scale 100% solar-wind renewable energy system. *Int. J. Hydrogen Energy* **2022**, *47*, 21613–21633. [CrossRef]
14. Xu, C.; Ke, Y.; Li, Y.; Chu, H. Data-driven configuration optimization of an off-grid wind/PV/hydrogen system based on modified NSGA-II and CRITIC-TOPSIS. *Energy Convers. Manag.* **2020**, *215*, 112892. [CrossRef]
15. Shahverdian, M.H.; Sohani, A.; Pedram, M.Z.; Sayyaadi, H. An optimal strategy for application of photovoltaic-wind turbine with PEMEC-PEMFC hydrogen storage system based on techno-economic, environmental, and availability indicators. *J. Clean. Prod.* **2022**, *384*, 135499. [CrossRef]
16. Hai, T.; Zoghi, M.; Abed, H.; Chauhan, B.S.; Ahmed, A.N. Exergy-economic study and multi-objective optimization of a geothermal-based combined organic flash cycle and PEMFC for poly-generation purpose. *Energy* **2023**, *268*, 126607. [CrossRef]
17. Zhao, P.; Gou, F.; Xu, W.; Shi, H.; Wang, J. Energy, exergy, economic and environmental (4E) analyses of an integrated system based on CH-CAES and electrical boiler for wind power penetration and CHP unit heat-power decoupling in wind enrichment region. *Energy* **2023**, *263*, 125917. [CrossRef]
18. Nasser, M.; Megahed, T.F.; Ookawara, S.; Hassan, H. Performance evaluation of PV panels/WT hybrid system for green hydrogen generation and storage: Energy, exergy, economic, and enviroeconomic. *Energy Convers. Manag.* **2022**, *267*, 115870. [CrossRef]
19. Hassan, H.; Yousef, M.S. An assessment of energy, exergy and CO_2 emissions of a solar desalination system under hot climate conditions. *Process Saf. Environ. Prot.* **2021**, *145*, 157–171. [CrossRef]
20. Manesh, M.H.K.; Rabeti, S.A.M.; Nourpour, M.; Said, Z. Energy, exergy, exergoeconomic, and exergoenvironmental analysis of an innovative solar-geothermal-gas driven polygeneration system for combined power, hydrogen, hot water, and freshwater production. *Sustain. Energy Technol. Assess.* **2022**, *51*, 101861.
21. Kalinci, Y.; Dincer, I.; Hepbasli, A. Energy and exergy analyses of a hybrid hydrogen energy system: A case study for Bozcaada. *Int. J. Hydrogen Energy* **2017**, *42*, 2492–2503. [CrossRef]
22. Kocer, A.A.; Ozturk, M. Thermodynamic analysis of power and hydrogen production from renewable energy-based integrated system. *Int. J. Exergy* **2016**, *19*, 519–543. [CrossRef]
23. Ahmadi, M.H.; Hosseini Dehshiri, S.S.; Hosseini Dehshiri, S.J.; Mostafaeipour, A.; Almutairi, K.; Ao, H.X.; Rezaei, M.; Techato, K. A thorough economic evaluation by implementing solar/wind energies for hydrogen production: A case study. *Sustainability* **2022**, *14*, 1177. [CrossRef]
24. Wang, J.; Dong, F.; Ma, Z.; Chen, H.; Yan, R. Multi-objective optimization with thermodynamic analysis of an integrated energy system based on biomass and solar energies. *J. Clean. Prod.* **2021**, *324*, 129257. [CrossRef]
25. Lu, C.; Wang, J.; Yan, R. Multi-objective optimization of combined cooling, heating and power system considering the collaboration of thermal energy storage with load uncertainties. *J. Energy Storage* **2021**, *40*, 102819. [CrossRef]

26. Heydari, A.; Nezhad, M.M.; Keynia, F.; Fekih, A.; Shahsavari-Pour, N.; Garcia, D.A.; Piras, G. A combined multi-objective intelligent optimization approach considering techno-economic and reliability factors for hybrid-renewable microgrid systems. *J. Clean. Prod.* **2022**, *383*, 135249. [CrossRef]
27. Bukar, A.L.; Tan, C.W. A review on stand-alone photovoltaic-wind energy system with fuel cell: System optimization and energy management strategy. *J. Clean. Prod.* **2019**, *221*, 73–88. [CrossRef]
28. Han, Z.; Wang, J.; Cui, Z.; Lu, C.; Qi, X. Multi-objective optimization and exergoeconomic analysis for a novel full-spectrum solar-assisted methanol combined cooling, heating, and power system. *Energy* **2021**, *237*, 121537. [CrossRef]
29. Liu, H.; Zhai, R.; Fu, J.; Wang, Y.; Yang, Y. Optimization study of thermal-storage PV-CSP integrated system based on GA-PSO algorithm. *Sol. Energy* **2019**, *184*, 391–409. [CrossRef]
30. Ruiming, F. Multi-objective optimized operation of integrated energy system with hydrogen storage. *Int. J. Hydrogen Energy* **2019**, *44*, 29409–29417. [CrossRef]
31. Pathak, D.P.; Khatod, D.K. Development of integrated renewable energy system based on optimal operational strategy and sizing for an un-electrified remote area. *IETE J. Res.* **2023**, *69*, 4531–4550. [CrossRef]
32. Zhang, T.; Wang, M.; Wang, P.; Gu, J.; Zheng, W.; Dong, Y. Bi-stage stochastic model for optimal capacity and electric cooling ratio of CCHPs-A case study for a hotel. *Energy Build.* **2019**, *194*, 113–122. [CrossRef]
33. Ding, Z.; Hou, H.; Duan, L.; Frate, G.F.; Zhang, N.; Desideri, U. Study on the capacity-operation collaborative optimization for multi-source complementary cogeneration system. *Energy Convers. Manag.* **2021**, *250*, 114920. [CrossRef]
34. Deymi-Dashtebayaz, M.; Baranov, I.V.; Nikitin, A.; Davoodi, V.; Sulin, A.; Norani, M.; Nikitina, V. An investigation of a hybrid wind-solar integrated energy system with heat and power energy storage system in a near-zero energy building—A dynamic study. *Energy Convers. Manag.* **2022**, *269*, 116085. [CrossRef]
35. Liu, L.; Zhai, R.; Hu, Y. Performance evaluation of wind-solar-hydrogen system for renewable energy generation and green hydrogen generation and storage: Energy, exergy, economic, and enviroeconomic. *Energy* **2023**, *276*, 127386. [CrossRef]
36. Liu, L.; Zhai, R.; Hu, Y.; Liu, S. Operation performance analysis of a novel renewable energy driven multi-energy supply system based on wind, PV, CSP, PEME and PEMFC. *Energy Technol.* **2023**, *11*, 2300291. [CrossRef]
37. Liu, L.; Zhai, R.; Hu, Y. Multi-objective optimization with advanced exergy analysis of a wind-solar-hydrogen multi-energy supply system. *Appl. Energy* **2023**, *348*, 121512. [CrossRef]
38. Dudley, V.; Kolb, G.; Mahoney, A.; Mancini, T.R.; Matthews, C.W.; Sloan, M.; Kearney, D. *Test Results SEGS LS-2 Solar Collector*; Sandia National Laboratories: Livermore, CA, USA, 1994.
39. Hochreiter, S.; Schmidhuber, J. Long short-term memory. *Neural Comput.* **1997**, *9*, 1735–1780. [CrossRef]
40. Laib, O.; Khadir, M.T.; Mihaylova, L. Toward efficient energy systems based on natural gas consumption prediction with LSTM Recurrent Neural Networks. *Energy* **2019**, *177*, 530–542. [CrossRef]
41. Wenya, L. Cooling, heating and electric load forecasting for integrated energy systems based on CNN-LSTM. In Proceedings of the 2021 6th International Conference on Power and Renewable Energy (ICPRE), Shanghai, China, 17–20 September 2021; pp. 808–812.
42. Ma, Z.; Chen, H.; Wang, J.; Yang, X.; Yan, R.; Jia, J.; Xu, W. Application of hybrid model based on double decomposition, error correction and deep learning in short-term wind speed prediction. *Energy Convers. Manag.* **2020**, *205*, 112345. [CrossRef]
43. EnergyPlus. Available online: https://www.energyplus.net/weatherlocation/asia_wmo_region_2/CHN/CHN_Hebei.Zhangbei.533990_CSWD (accessed on 15 April 2022).